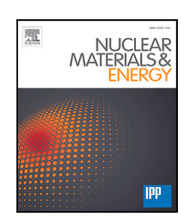
FISEVIER

Contents lists available at ScienceDirect

# **Nuclear Materials and Energy**

journal homepage: www.elsevier.com/locate/nme





# Evolution of radiation profiles in a strongly baffled divertor on MAST Upgrade

Fabio Federici a, Matthew L. Reinke, Bruce Lipschultz, Jack J. Lovella, Kevin Verhaegh, Nicola Lonigro, Cyd Cowley, Mike Kryjak, Peter Ryan, Peter Ryan, Andrew J. Thornton, James R. Harrison, Byron J. Peterson, Bartosz Lomanowski, Byron D. Lore, Yacopo Damizia, the EUROfusion Tokamak Exploitation Team, the MAST Upgrade team.

- a Oak Ridge National Laboratory, Oak Ridge, TN 37831, USA
- <sup>b</sup> Commonwealth Fusion Systems, Cambridge, MA 02139, USA
- <sup>c</sup> York Plasma Institute, University of York, Heslington, York, YO10 5DD, UK
- d UK Atomic Energy Authority, Culham Centre for Fusion Energy, Abingdon, OX14 3DB, UK
- e digiLab, The Quay, Exeter EX2 4AN, United Kingdom
- f National Institute for Fusion Science, 322-6 Oroshi-cho, Toki 509-5292, Japan
- 8 Electrical Engineering and Electronics department, University of Liverpool, Liverpool, L69 3GJ, UK

# ARTICLE INFO

# Keywords: Detachment DLS model Radiation detachment Roll-over IRVB Confinement Impurity power losses

# ABSTRACT

Plasma detachment in tokamaks is necessary in future tokamaks to sufficiently reduce the heat flux to the target. It involves interactions of the plasma with impurities and neutral particles, leading to significant losses of plasma power, momentum, and particles. An accurate mapping of plasma emissivity in the divertor and X-point region is essential to localise and infer the power losses influencing the detachment process. The recently validated InfraRed Video Bolometer (IRVB) diagnostic, in MAST-U (Federici et al., 2023), enables this mapping with higher spatial resolution than more established methods like resistive bolometers.

In previous preliminary work (Federici et al., 2023a), the detachment of the radiation from the target (radiative detachment) was characterised in L-mode (power entering the scrape-off layer,  $P_{SOL} \sim 0.4$  MW). With a conventional divertor the inner leg consistently detached ahead of the outer leg, and radiative detachment preceded particle flux detachment. This work presents results also from the third MAST-U experimental campaign, fuelled from the low field side instead of the high field side, including Ohmic and beam heated L-mode shots (with a power exiting the core up to  $P_{SOL} \sim 1-1.5$  MW).

The radiation peak moves upstream from the target at lower upstream densities than the ion target flux roll-over (typically considered the detachment onset), while radiation on the inner leg detaches before the outer one in high field side fuelled shots and about at the same time in low field side fuelled ones. The movement of the radiation is in partial agreement with the expectations from the DLS model (Myatra, 2021; Cowley et al., 2022; Lipschultz et al., 2016), predicting a sudden shift from the target to the X-point on the inner leg. The energy confinement is found to be related to detachment, but there seems to be some margin between the radiation peak caused by impurity radiation reaching the X-point and confinement being affected, a beneficial characteristic if it could be extrapolated to future reactors. For increasing  $P_{SOL}$  the particle flux roll-over happens for similar upstream densities. Comparing the total radiated power with the  $D_2$  Fulcher band emission evolution shows that in a conventional divertor a significant fraction of the radiated power is due to carbon radiation (outside of the divertor chamber).

E-mail address: fabio.federici@ukaea.uk (F. Federici).

<sup>\*</sup> Corresponding author.

<sup>&</sup>lt;sup>1</sup> See author list of E. Joffrin et al. 2024 Nucl. Fusion (https://doi.org/10.1088/1741-4326/ad2be4).

<sup>&</sup>lt;sup>2</sup> See author list of J. Harrison et al. 2019 Nucl. Fusion 59 112011 (https://doi.org/10.1088/1741-4326/ab121c).

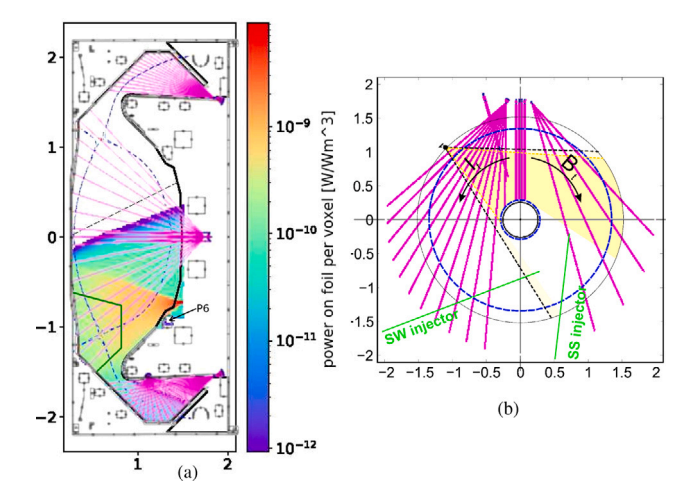


Fig. 1. Poloidal (a) and top (b) view of MAST-U, showing the comparison of the resistive bolometer system LOS (magenta) with (a) a colour plot obtained by scanning all the voxels with a 1 W/m $^3$  emitter and integrating the power absorbed by the foil, indicating the regions of higher sensitivity of the IRVB, and (b) the edges of the FOV (yellow, mostly counter-NBI). In (b) is also the position of neutral beam injectors (NBI, green). Adapted from [6,7]. For reference the separatrix of a typical plasma is shown as an overlay of a blue dashed line. The FOV for MU02 and MU03 is shown and the edges of the MU01 FOV are shown with dashed black lines. The region delimitated by the green solid line indicates voxels with a good tangential and poloidal view, therefore the regularisation of the inversion is reduced and resolution increased. For interpretation of the references to colour in this figure legend and all the following, the reader is referred to the web version of this article.

# 1. Introduction

MAST-U is a spherical tokamak at the Culham Centre for Fusion Energy (CCFE) in the United Kingdom [1,2]. It features a double null (DN) plasma, strongly baffled divertor configurations, and can support an innovative Super-X divertor (SXD), which significantly reduces outer target heat loads and improves access and stability of plasma (e.g. 'particle') detachment [3–5].

In this work, we investigate the radiative power dissipation and its evolution as detachment progresses on MAST-U. To accurately measure the total radiative emissivity profile, multiple resistive bolometer arrays are installed to monitor the core and divertor chamber. To complement the resistive system and fill the gap from the X-point to the divertor chamber (see Fig. 1), a prototype Infrared Video Bolometer (IRVB) was installed, aimed at the lower X-point. This diagnostic was recently validated [8] and its data have already been used to complement various scientific endeavors [3,5,9-11]. Until now, the resistive system has been affected by significant noise that, while still allowing the calculation of the total radiated power from the core, prevented detailed measurements of the movement of the radiation front in the divertor chamber. Although the IRVB cannot reconstruct the radiative emissivity map in the Super-X divertor chamber, due to its viewing location, its field of view (FOV) is adequate for investigating the radiative emissivity distribution in the Conventional Divertor (CD) configuration [7].

This paper presents the initial results from the analysis of the IRVB data from the first MAST-U experimental campaign (MU01) and third (MU03) L-mode CD shots focusing on changes in the total radiated power spatial distribution along the divertor legs in connection with detachment.

Usually, when the plasma is attached to the target in high recycling a region with strong thermal gradients (thermal front), high total radiative emissivity and high ionisation rate is present on the divertor legs close to the strikes points [12]. The radiation is due to volumetric processes like hydrogen/impurities electron-impact excitation. These strongly depend on the impurities species and the temperature/density profiles in the plasma [13] . When the core density increases, the target

temperature decreases while the target electron density and ion flux increase, maintaining a similar plasma pressure all along the separatrix. After the target temperature reaches a certain threshold (usually 3-5 eV [3,14]), volumetric momentum losses begins to occur and the ion target flux decreases (a classical marker for detachment onset). A region of low temperature grows at the target and the plasma pressure decreases within this region. We will refer to the region where the pressure starts decreasing as detachment front. This is usually related to the ionisation front, the downstream edge of the region with strong ionisation [5]. The thermal front and the radiation associated with it also move upstream towards the X-point ('detach' from the target) along the separatrix. If the radiation comes mainly from hydrogenic processes, the thermal front movement will be approximatively aligned with the ionisation/detachment front. If the dominant source of radiation involves impurities, that radiate the most at higher temperatures, then the peak emission could recede from the target and move upstream before detachment occurs [15]. Thermal front detachment was the subject of significant modelling efforts using simplified analytical models, among which is the detachment location sensitivity (DLS) model, which aims to predict the location and sensitivity of the thermal front location [12,16,17]. Assuming the thermal front and the region with peak emission coincide, we will compare this prediction with experimental observations. The movement of the thermal front (represented by the 3-5 eV temperature region) was investigated with MAST-U Super-X interpretative SOLPS simulations, noting that it matches the movement of the  $D_2$  Fulcher emission front from experiments [3]. The Fulcher emission is then correlated with the ionisation front [4]. In MAST-U Super-X chamber the main source of radiation is hydrogenic, so this also coincides with the peak radiation [5,7].

#### 2. Diagnostic improvements

Before discussing our experimental results, we will first discuss the IRVB diagnostic implementation and its various improvements. IRVB measurements first started in MU01, further documented in Refs. [7,8]. The geometry of the IRVB was optimised in MU02 to provide a more detailed view of the plasma around the X-point by retracting the foil from the pinhole, from 45 mm to 60 mm. As a downside, now the FOV extends up to  $\sim$ 15 cm below the midplane. This makes it harder to observe high field side (HFS) MARFE-like structures, but these are usually poloidally extended enough to still be visible. A significantly thinner platinum absorber foil than expected (measured  $\sim 0.72 \mu m$ instead of nominal 2.5) [18] resulted in higher signal levels than expected [8], enabling this modification. The IRVB geometry optimisation also reduced the portion of the foil shaded by the P6 coil (see Fig. 1) and increased the coverage of the divertor chamber (Figure 2.5a to 2.5b in [7]). The IRVB geometry was verified to improve the accuracy of the geometrical calibration beyond the design specification. The internal pinhole location was accurately triangulated with sub-mm precision with CALCAM fits from multiple angles [19], returning a ~3.9 mm shift with respect to the target parameter. Together with the exact location of the IRVB flange on the vacuum vessel, the precise FOV for MU02, MU03, and the future MU04 was determined, shown in Fig. 1. This improved IRVB FOV characterisation has greatly improved the accuracy of IRVB measurements, enabling it to distinguish if radiation is at or slightly (a few cm) away from the plasma surface facing components in the divertor.

After a camera image is obtained by the IRVB, a Bayesian tomographic inversion is performed to obtain a 2D radiative emissivity map [7]. This inversion is performed with an arbitrary regularisation coefficient to reduce noise on the inversion. Unlike previous results, spatial binning of the camera pixels has been disabled, improving the inversion by making use of the full resolution available from the camera. Additionally the regularisation is reduced for the region that can be well imaged in both the poloidal and tangential views, delimitated by a green line in Fig. 1(a), allowing for a higher spatial resolution. A running average smoother (~30 ms) is applied over time to remove temporal oscillations presented previously [8], hence the data will be presented with such time resolution.

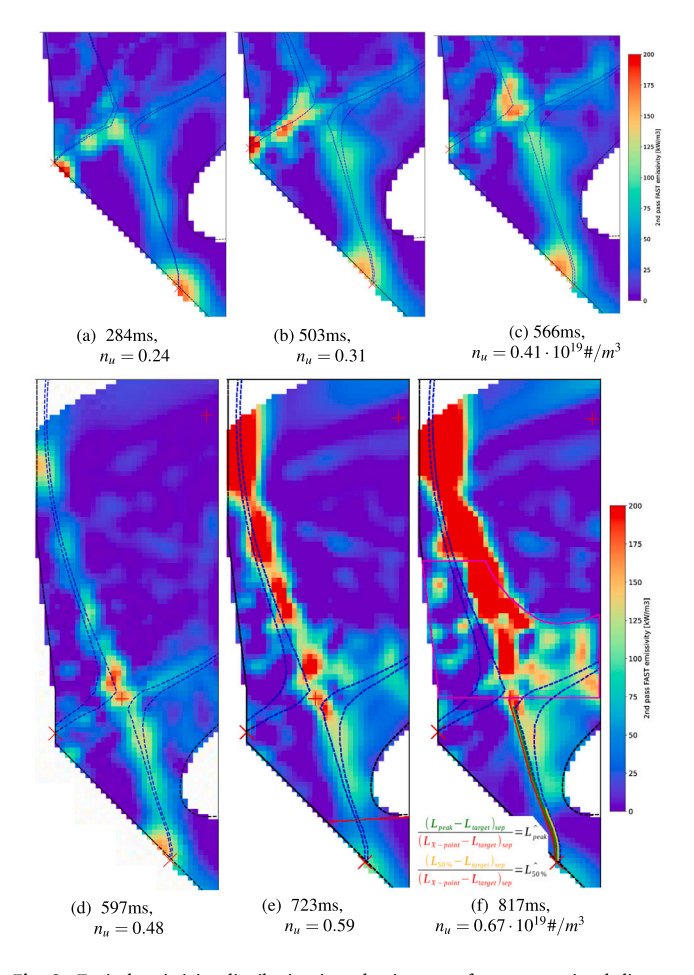


**Fig. 2.** Typical emissivity distribution in a density ramp for a conventional divertor, L-mode, HFS fuelled, Ohmic plasma (shot 45473, DN and  $I_p = 600$  kA, same used in [8]). First, both inner and outer targets are radiatively attached (a), then the inner detaches (b) up to the X-point (c). Further increasing the density a radiation MARFE-like structure start to grow on the high field side (HFS) midplane with the outer leg still attached (d), then the outer leg starts detaching (e) and the radiation on the separatrix moves further inward the core (f) leading to a disruption. Note that all images have the same bar ranges. In e the red line in the divertor indicates the approximate upper bound of the DMS LOSs and MWI FOV. In (f) is also shown the definition of  $\hat{L}_{peak}$  and  $\hat{L}_{50\%}$ . The purple line indicates the are used to calculate the radiation baricentre in the core.

# 3. Typical total emissivity results

L-mode DN shots are analysed in this paper, as upstream conditions are difficult to control in H-mode. The data is from the MU01 and MU03 campaigns. The only impurity present in significant quantities is the intrinsic carbon from the walls.

MU01 was the first experimental campaign in MAST-U and it was often characterised by the presence of MHD activity (possibly influenced by error fields) and imprecise plasma positioning control, which negatively affected the overall plasma performance (shots 45 468, 45 469, 45 470, 45 473). The shots are Ohmically heated with fuelling from the HFS, have a plasma current  $I_p = 600$  kA and have a power crossing the separatrix ( $P_{SOL}$ )  $\sim$ 0.4 MW (determined as the Ohmic power minus the power radiated in the core measured by resistive bolometry).

In MU03 similar shots were performed with a more optimised scenario, yielding better overall performance. They are characterised by a higher starting density, so the transition of the radiation detaching on both legs cannot be observed (shots 47 950, 47 973, 48 144). The shots are Ohmically heated with main fuelling from the low field side (LFS),  $I_p = 750 \text{ kA}$  and  $P_{SOL} \sim 0.5 - 0.6 \text{ MW}$ .

LFS fuelling was employed to enable higher power L-mode operation, making the scenario compatible with off-axis (SW) 1.5–1.8 MW NBI heating [15] by disrupting the pedestal flow shear hence raising the L-H threshold. These beam-heated L-mode discharges allow us to verify if the detachment evolution changes with a higher  $P_{SOL}$  and were meant to better probe the initial stages of detachment (at higher  $P_{SOL}$  a higher  $n_u$  is expected to be required to achieve detachment), featuring  $I_p = 750$  kA and  $P_{SOL} \sim 1-1.5$  MW.

First we will describe the typical evolution of the radiative emissivity during a core density ramp where the divertor is progressively cooled. A typical MU01 discharge with HFS fuelling is shown in Fig. 2.

The peak of the radiated power is initially at the strike points. Increasing the upstream density a second region with high emissivity forms on the inner leg close to the x-point, while still some is present at the target (Fig. 2(b)). The second region could be due to processes like electron-impact excitation (EIE) of deuterium or impurities, that can occur in the volume at intermediate temperatures, happening upstream as the target temperature decreases. Processes like recombination instead occur at lower temperature. Progressively the target emission diminishes and ultimately disappears, while the emission upstream increases and moves closer to the x-point. During this period the emission in the outer leg still remains peaked at the target, albeit slightly increasing upstream. This shows that the radiation region detaches from the inner target consistently at lower densities than the outer target. The outer leg dissipates significantly more power than the inner one, even if it has often lower emissivity, due to its larger volume integral (at least 5 times). After the inner leg radiation reaches the X-point, it progresses upstream towards the midplane along the inner separatrix. A MARFElike structure appears at the HFS midplane even before the outer leg radiatively detaches. This is likely caused by HFS fuelling, as the inner gap (~4 cm) is sufficiently large to avoid interactions with the HFS column and this phenomenon does not occur in shots fuelled from the LFS (MU02 and MU03). During this transition, the radiation on the outer leg gradually recedes from the target, ultimately reaching the Xpoint. This is not characterised by bright regions sharply separated as for the inner leg, even is this could be an artefact due to the inversion smoothing. For this HFS fuelled discharge with a conventional divertor, the transition on the outer leg happens at the same time or after the MARFE appears, potentially indicating that the cause of its detachment could be a  $P_{SOL}$  reduction due to the additional power losses due to the MARFE.

The presence of the MARFE-like structure is also observed in interpretative SOLPS simulations [3] and is confirmed by high speed visible imaging, Thomson scattering (TS) measurements (that shows a region of high density and low temperature penetrating the core from the HFS midplane) and resistive bolometry (increased brightness of the LOS close to the central column). The latter is routinely used to verify if a peaked emission close to the inner midplane in the IRVB inversions constitutes an artefact or a true MARFE-structure occurrence (artefacts are more common with the MU02 and onwards optimised IRVB FOV).

When the radiation reaches the proximity of the last closed flux surface the spatial resolution is insufficient to distinguish if this is in the core or in the scrape-off layer (SOL, Fig. 2(d)). Further increasing the electron densities instead causes a clear inward movement of the radiation on the separatrix between midplane and X-point towards the core (compare Fig. 2(e) with Fig. 2(f)).

A typical MU02/3 discharge with LFS fuelling and a conventional divertor is shown in Fig. 3. The movement of the radiation on the inner leg happens in a similar fashion as for HFS fuelled shots. Radiation is present initially both at the target as close to the X-point, with a larger spacing appearing between the two. This could be due to a different behaviour of the plasma or diagnostic. The small change in divertor geometry between MU01 and MU02 causes the second inner leg peak in Fig. 2(b) to correspond to a portion of the IRVB foil with slightly different properties, potentially exacerbating this difference. A more significant difference is that the radiation reduction on the outer leg

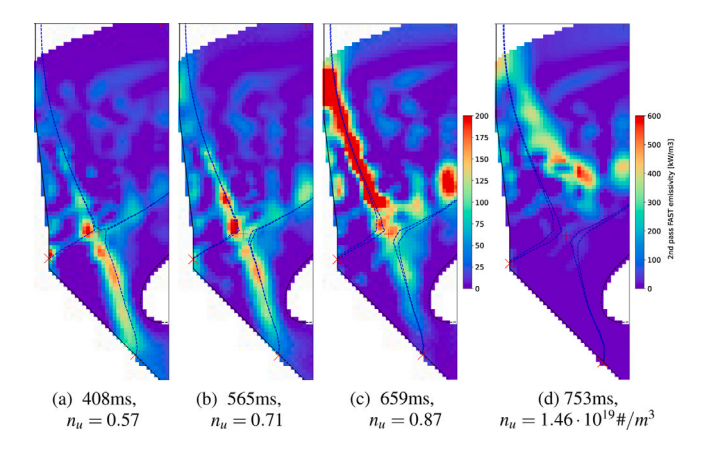


**Fig. 3.** Typical emissivity distribution in a density ramp for a conventional divertor, L-mode, LFS fuelled, Ohmic/beam heated plasma (shot 48144, DN and  $I_p=750$  kA). The initial density is not low enough for either leg to be initially completely attached. Emission is present on the inner leg close to the x-point, as the peak on the outer leg not being localised at the target (a). The inner then leg completely radiatively detaches (b). At further higher density the outer leg radiative detachment continues while a strong radiation appears between X-point and midplane on the HFS separatrix (c). Then the radiation moves progressively inside the core, with no formation of the MARFE (d). Note that the mission close to the HFS midplane in (c, d) resembling a MARFE is instead a tomographic inversion artefact. (a, b, c) have the same bar ranges.

target happens while the radiation on the HFS is still close to the X-point (see Fig. 3(a)). This could indicate that detachment could instead be due to increased recycling as in the classical picture of the process. For increasing density the radiating region further detaches from the targets while emission grows on the HFS separatrix. Here no MARFE happens, and the core emission is a broad poloidally aligned emitting region centred around the X-point. The emission on the HFS midplane in contact with the central column in Fig. 3(c), d resembling a MARFE is instead a tomographic inversion artefact. This regime does not appear to correspond to an X-point radiator, given the large poloidal extent of the radiation feature [20].

# 4. Model predictions

Our aim is to compare the movement of the total radiation distribution against model predictions. The Two Point Model (2PM) [21] was modified to include the presence of a thermal front in the Thermal Front Model [22]. This model was further refined to consider the leg geometry and magnetic field, resulting in the Detachment Location Sensitivity (DLS) model [12]. In the DLS and other models, the thermal front is defined as a narrow region where "the electron temperature transitions between the hotter upstream region and the colder region below which is dominated by ionisation, recombination, and other neutral processes" [12]. This region is associated with high total radiated power, usually attributed to the presence of impurities in the plasma that radiate efficiently at the temperature typical of the SOL and divertor, that constitute the dominant power loss mechanism. The front is idealised in the DLS model as narrow, so the (impurity) radiation front and the ionisation (detachment) front location is practically the same. In reality this is not the case and a clear separation between the impurity radiation region and the ionisation/detachment front is observed [15,23]. Furthermore, the emissivity seldom has a single well defined peak that identifies the radiation front.

The DLS predicts that for given magnetic geometry (e.g. different inner and outer leg topologies (CD, Super-X)) the location of the thermal front depends on the control parameter  $C = \frac{n_u \sqrt{f_I}}{q_{\parallel u}^{S/I}}$ , containing

upstream conditions (upstream heat flux  $q_{\parallel,u}$ , upstream electron density  $n_u$ ) and the divertor impurity concentration  $f_I$ . The impact of the

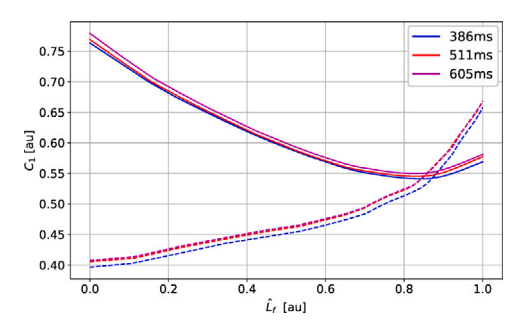


**Fig. 4.**  $C_1$  parameter variation in shot 45473 for a front position from target  $(\hat{L}_f=0)$  to X-point  $(\hat{L}_f=1)$ . Solid lines for inner leg, dashed for outer [7].

magnetic geometry on the thermal front location can be quantified via the coefficient  $C_1(s_{\parallel,f}) = \frac{B_f}{B_u} \left[ \int_{s_X}^{L_\parallel} \frac{B(s_\parallel)}{B_X} \frac{(L_\parallel - s_\parallel)}{(L_\parallel - s_X)} \, ds_\parallel + \int_{s_{\parallel,f}}^{s_X} \frac{B(s_\parallel)}{B_X} \, ds_\parallel \right]^{-2/7}$ 

where  $s_{\parallel}$  is the position along the separatrix and f denotes quantities at the front location [17] ( $S_{\parallel,f}=0$  corresponds to the thermal front at the target: the detachment onset). Assuming a constant electron heat conductivity coefficient and radiative cooling function (it depends on the impurity species and their transport),  $\frac{n_u \sqrt{f_I}}{q_{\parallel,f}} \propto C_1$ . Therefore,

the front location can be modelled as function of magnetic geometry  $C_1(s_{\parallel,f})$  in terms of changes in  $n_u$ ,  $f_I$ ,  $q_{\parallel,u}$ . If  $f_I$  and  $P_{SOL}$  are constant and the MAST scaling law between power decay length at the outer midplane  $(\lambda_q)$  and  $n_u$  from [24] is used, this further reduces to  $n_u^{1.5} \propto C_1(s_{\parallel,f})$  [23]. The sensitivity and stability of the detachment front at a certain location  $(s_{\parallel,f})$  can be modelled as  $\frac{dC_1}{ds_{\parallel,f}}$ . If  $C_1$  decreases from the target to the X-point  $(\frac{dC_1}{ds_{\parallel,f}} < 0)$ , the detachment front location

is unstable, as a slight perturbation towards the X-point increases the power dissipated in it, pushing the front further upstream. Conversely,  $\frac{dC_1}{ds_{\parallel,f}}>0$  implies an intrinsic detachment front stabilisation.

For a typical MAST-U CD configuration, the  $C_1$  profile along the inner and outer divertor leg is shown in Fig. 4. The front on the inner leg is unstable up to a location very close to the X-point, while the front on the outer leg is stable. This model behaviour can be verified with IRVB measurements.

# 5. Front characterisation

To compare the DLS predictions with the IRVB data, it is essential to define how to identify the thermal front from the total radiated power profile. A simple way, using the definition from the DLS model itself, is to identify the front as the region with the peak emissivity along a divertor leg and thus the highest radiative dissipation, the 'peak radiation front'. The current MAST-U IRVB implementation, though, is characterised by significant non-uniformities of the absorber foil properties [8], which causes local variations affecting in particular the peak emissivity obtained from the tomographic inversion. Rather than moving smoothly the peak radiation is observed to jump between neighbouring points, see how the radiation moves on the outer leg in Fig. 3. Foil non-uniformities are planned to be reduced in the future by replacing the foil with one produced with vapour deposition processes [18]. Additionally, the radiation can have multiple peaks, as described in Section 3 on MAST-U as both impurity radiation and, downstream, hydrogen EIE results in significant radiative power losses [15]. EIE is the largest contributor to the total radiated power within the Super-X divertor chamber (in a detached plasma without extrinsic impurity seeding [5,15]). For these reasons it can be difficult to identify which is the dominant radiation peak and pinpoint exactly its origin. Another metric that can be used is the location where the

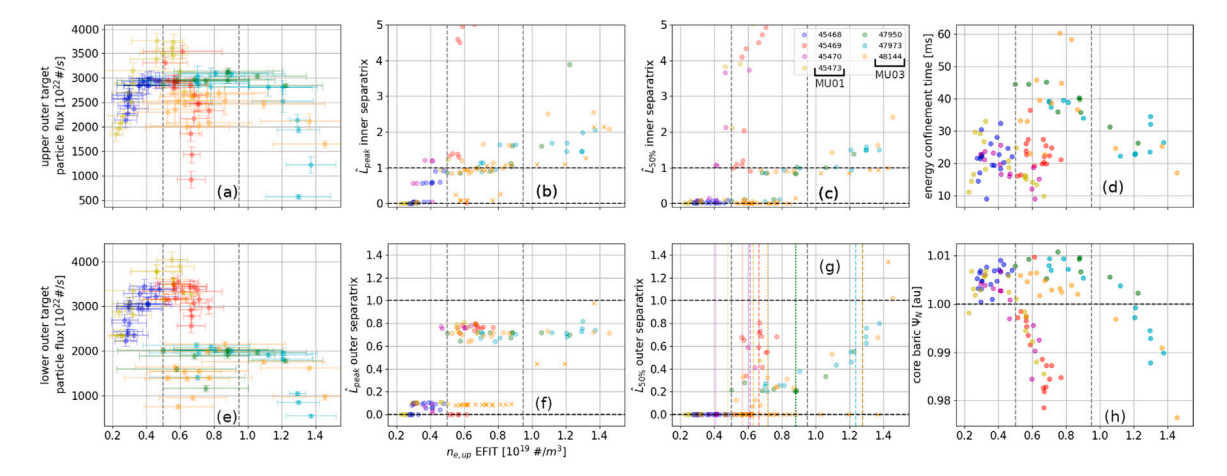


Fig. 5. (a) upper and (e) lower target current, providing the detachment condition from particle flux roll-over compared to the upstream density determined using Thomson scattering (TS) and EFIT. (b) movement of the radiated emission peak and (c) of the region with emissivity of 50% of the peak on the separatrix, both indicating radiative detachment, in the inner leg and (f, g) lower leg. When available, the analogous data from the XPI/MWI  $D_2$  Fulcher emission inversions is shown in crosses. In (g) vertical and dashed lines indicate the start and end of the decrease of the  $D_2$  Fulcher emission from the DMS line of sight at the outer strike point respectively, while the dotted line the decrease of the  $D_2$  Fulcher emission from MWI. (d) energy confinement time and (h)  $\Psi_N$  baricentre of the radiation within the purple region in Fig. 2(f) variation with upstream density. Data referring to Ohmic heated L-mode shots. The first 4 cases are from MU01 with HFS fuelling,  $I_p = 600$  kA and  $P_{SOL} \sim 0.5$ —0.6 MW. The vertical black dashed lines indicate the approximate particle flux roll-over.

radiation has a sharp decrease downstream of the peak towards the target. This can be tracked more reliably than the peak emission. If along a leg two peaks of similar height are present the highest can be either, and the location of the peak jump accordingly, while the region with sharp decrease will still be the same on the side of the most downstream peak. If hydrogenic radiation is at least comparable with the impurity driven one, the region with sharp radiation decrease is likely reminiscent of the cold side of the thermal front, where  $T_e$  becomes too low (<3–5 eV) for EIE (that dominates hydrogenic radiation) and ionisation [5]. This region is tracked experimentally by tracking the location where the radiative emissivity reaches a set fraction (50% is used here, hence '50% radiation front') of the peak emission in the divertor leg, analogous to techniques that have tracked the ionisation front using imaging [25–28].

The peak radiation front corresponds to the peak in total radiation (hydrogenic + impurity), whose movement we define as the beginning of 'radiative detachment'. The plasma is radiatively fully detached when 50% radiation front recedes from the target moving upstream. In the remainder of the paper, both radiation fronts are tracked in terms of poloidal distance from the target along the separatrix divided by the poloidal distance from the X-point to target, see Fig. 2(f) for the definition: 0 corresponds to the target, 1 corresponds to the X-point, >1 implies locations upstream of the X-point towards the midplane. It should be noted that given the IRVB FOV, the radiation cannot be reliably tracked on the outer separatrix above the X-point.

To put the evolution of these two radiative power markers into perspective, their evolution is compared with the total target particle flux. Before particle detachment, the target particle flux first increases as the upstream/core density is increased, as predicted by the 2PM. Due to a combination of power limitation, volumetric recombination and momentum losses, the particle flux first plateaus (detachment onset) and then decreases or 'rolls-over' (detachment). In MAST-U, Langmuir probes (LPs) are used to monitor the particle flux, and they are present only at the outer strike points (both upper and lower in DN) [29].

The detachment of the ionisation region from the target can be observed more directly using the  $D_2$  Fulcher band emission front as a proxy for the ionisation region [4,27,28,30,31]. For a CD, this can be observed by monitoring the brightness of the  $D_2$  Fulcher emission near the strike point, using in MAST-U the Divertor Monitoring System diagnostic (DMS) [4], the Multi Wave Imaging system (MWI) [32], and X-Point Imaging system (XPI) [15,23,33]. The DMS can only observe the  $D_2$  Fulcher emission in the lower outer divertor chamber, thus near

the outer strike point (see the red line in Fig. 2(e)). It typically increases or remains constant in attached conditions. Then as density increases the emission reduces sharply at some point in the conventional divertor [23]. This is related to the detachment of the ionisation front, as previously mentioned. For the shots where this data is available, the upstream density at which the D2 Fulcher emission starts decreasing and reaches the minimum are recorded and shown in Fig. 5g and 6g as solid and dashed lines respectively. The MWI too can only observe the emission in the lower outer divertor chamber, thus near the outer strike point for the conventional divertor. Here I record the moment where the  $D_2$  Fulcher emission starts to decrease and goes below an arbitrary threshold, and will be shown as a vertical dotted line. The XPI has a field of view similar to the IRVB and can therefore monitor both the inner and outer legs. Combining the data from the MWI a tomographic inversion of the entire lower divertor can be performed. With this data it is possible to track the movement of the peak and 50% thresholds in a way completely analogous to what is done with the total radiated power. This data will be shown as crosses in Figs. 5 and 6 b,c,f,g.

Finally, a movement of the radiation front upstream implies that a region of 'cold' plasma moves towards the core. Work on other tokamaks has shown that core confinement may deteriorate when this radiation front is near the X-point and, subsequently, enters the core [34–36]. Such core deterioration is detrimental for future fusion reactors. To monitor this, we compare the evolution of detachment with the energy confinement time,  $\tau_{th}$ , defined by  $\frac{dW}{dt} = P_{heat} - \frac{W}{\tau_{th}}$  with W the stored energy and  $P_{heat}$  the power injected in the core. Additionally the  $\Psi_N$  of baricentre of the total emission is calculated in the region  $-0.6 < Z < Z_{X-point}$  and  $0.9 < \Psi_N < 1.1$  (see Fig. 2(f)). The first limitation is to avoid the MARFE artefact sometime appearing in MU02/03 shots and only above the X-point, the second is to monitor the radiation only close to the separatrix. Even if the uncertainties in the spatial location of the radiation are present, the general trend can be observed.

# 6. Front tracking results

After having discussed the general evolution of the radiative emissivity and defined our two different radiative front identifiers, we show their evolution as function of upstream density at the outer separatrix midplane ( $n_{e,up}EFIT$ ).  $n_{e,up}EFIT$  is obtained from smoothed Thomson scattering (TS) data and the location of outer midplane separatrix from EFIT [37]. An important caveat to this technique is that  $n_{e,up}EFIT$ 

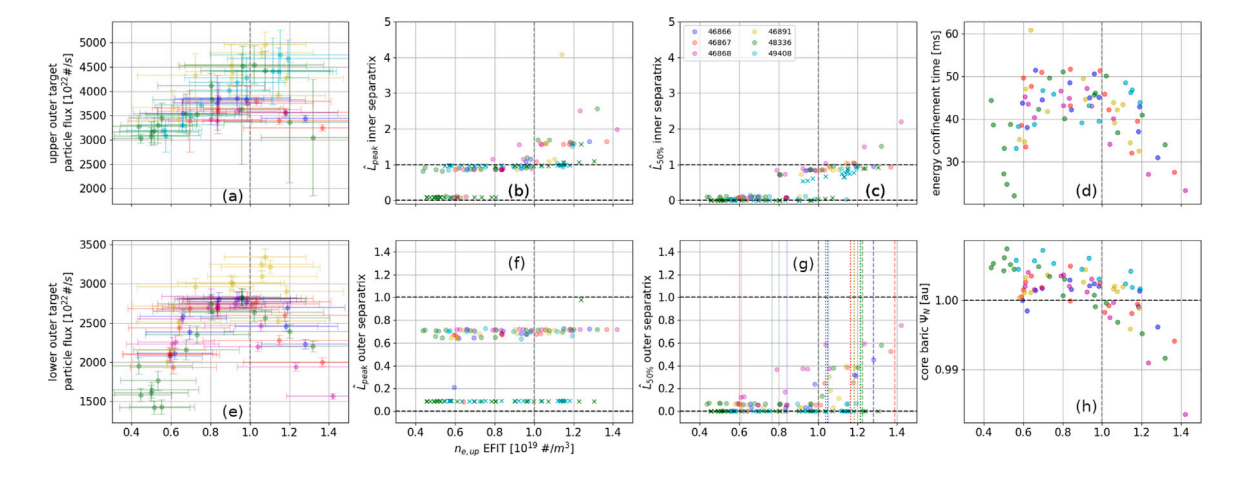


Fig. 6. The quantities are the same as in Fig. 5. Data referring to beam heated L-mode shots ( $P_{SOL} \sim 1-1.5$  MW) fuelled from the LFS and  $I_p = 750$  kA.

has large uncertainties due to the uncertainty of the separatrix position determination. Although this can cause systematic uncertainties between different discharges, the trend here identified by  $n_{e,up}EFIT$  should be relatively reliable, as similar dependencies are found in terms of Greenwald fraction. The uncertainty here shown associated with  $n_{e,up}EFIT$  is derived from the uncertainty in the match between IRVB time and machine time (+10/-15 ms), but mainly from an arbitrary 1 cm uncertainty in the separatrix location at the LFS midplane.

Fig. 5 shows the results for the MU01 and MU03 Ohmic shots, which are compared separately in the following.

In MU01 HFS fuelled shots, the roll-over is quite clear on both outer strike points, happening at  $n_{e,up}EFIT\sim0.5\times10^{19}$  #/m³, and the particle flux is quite up/down symmetric. This is the case even if in these shots  $dr_{sep}$  (the distance between the two separatrix, associated with the upper and lower X-points, at the outer midplane; if positive the last closed flux surface delimiting the core is the one connected with the upper X-point and vice versa) gradually decreases from 0 to -6 mm, with  $\lambda_q$  in the range 5–15 mm (consistent with MAST scaling laws [24]). Such a large  $dr_{sep}/\lambda_q$  ratio is expected to cause significant heat flux asymmetries [38], which seems to be inconsistent with the particle flux symmetry and the lack of asymmetries observed in high speed camera data or resistive bolometry measurements. This may indicate inaccuracies in the  $dr_{sep}$  retrieved from EFIT for MAST-U, larger  $\lambda_q$  than currently determined or expected from scaling laws, or be due to power redistribution via drifts [39].

The start of the peak radiation movement from the outer target across all MU01 discharges happens at a similar  $n_{e,up}$  outer targets particle flux roll-over, while the inner peak radiation detaches slightly earlier. The movement of the peak radiation is not regular for both divertor legs (clustering around 0/0.6/~1 on the inner leg and 0/0.75 on the outer), likely due to the foil non uniformity previously mentioned. The 50% falloff marker on the inner separatrix reaches the HFS midplane about when the peak radiation detaches from the outer target. The evolution of the 50% falloff marker is very gradual on the outer divertor leg, in contrast to the inner leg where the radiation quickly disappears from the target and re-appears near the X-point (e.g. there are almost no points between  $\hat{L} = 0$  and 1). This abrupt movement of the radiation on the inner leg, but not on the outer leg, is in agreement with the DLS model prediction in Section 4, of a stable detachment on the outer leg and unstable detachment on the inner leg. Further research is required using post MU02 discharges where the IRVB viewing geometry was fully verified to obtain higher confidence in this conclusion. The detachment of the ionisation front from the DMS  $D_2$  Fulcher emission starts on the outer leg together with the particle flux roll-over and movement of the peak radiation, while it ends at the same time as the movement of the 50% radiation marker. The fact that on the outer leg the total radiation movement aligns well with the  $D_2$  Fulcher emission can indicate that hydrogenic radiation is there a significant power loss mechanism. Lastly, the confinement time initially increases due to the increase in stored energy at the beginning of the shot, but as soon as the peak radiation moves from the inner target there is a strong degradation. This is true also for the ratio of  $\tau_{th}$  with the confinement time from scaling laws identified in [7]. In the related plot of the core  $\Psi_N$  baricentre it can be seen that the radiation penetrates the core gradually, surpassing the separatrix when the radiation fully detaches from the inner target. This can indicate that the initial core performance degradation is due to the localised cooling at the fuelling location, and afterwards the cold region becomes more poloidally more diffused, further worsening confinement.

LFS fuelled MU03 Ohmic shots have higher  $I_p$  and  $P_{SOL}$  and reduced interactions with the main vessel and baffle plates. This increases the particle flux roll-over point from a Greenwald fraction of 0.22 to 0.35. Although |  $dr_{sep}$  |  $/\lambda_q$  is reduced (e.g. |  $dr_{sep}$  |< 1 mm with  $\lambda_q$  between 5–15 mm), the LPs measure a noticeably higher particle flux on the upper outer leg. This is consistent with recent experiments and simulation studies that indicate significant up/down asymmetries in the MAST-U plasma due to drifts in a connected DN, although further studies are required — particularly given the uncertainty of  $dr_{sep}$  [39,40]. The initial upstream density is not low enough to witness the detachment of the peak radiation on either leg, but the 50% falloff still detaches from both targets at similar  $n_{e,up}$ , if not earlier on the outer, much earlier than the outer target particle roll-over. The distinct separation between the movement of the peak radiation and the 50% radiation marker/particle flux roll-over is very significant, as indicates that while the hydrogenic radiative losses are important, the peak radiative emissivity is determined impurity radiation, most likely carbon. This is further confirmed by the DMS and MWI observations. which show the detachment of the  $D_2$  Fulcher emission on the outer leg to happen slightly after the detachment of the 50% radiation marker. Finally, the XPI/MWI  $D_2$  Fulcher emission inversions clearly show too the movement of their peak and 50% markers to be closely related with the 50% radiation marker. This is significant as it shows the importance of carbon radiative losses in MAST-U, contrary to what is generally observed in the Super-X chamber [5,7]. The match is closer on the inner leg, while  $D_2$  Fulcher emission detaches quite later on the outer leg. A sharp transition of the radiative  $\hat{L}_{50\%}$  from 0 to 1 is observed on the inner leg while the  $\hat{L}_{50\%}$  evolution is more gradual on the outer leg, in agreement with older MU01 results. This also true for the XPI/MWI  $D_2$  Fulcher emission. It should be noted, however, that the ionisation front movement is much faster for the conventional divertor than for the Super-X divertor, as its detachment sensitivity is higher [23,28].3 When the outer leg radiation reaches the X-point, the radiation on the inner separatrix rises further upstream. Apart from the very end of shot 47950, there is no evidence of the presence of a MARFE-like structure localised at the HFS midplane from both IRVB and resistive bolometry. The lack of such a MARFE structure, likely driven by the difference in fuelling, results in less degradation of  $P_{SOL}$  with a more "normal" evolution of detachment, occurring over a much larger range of upstream density. The energy confinement time is increased compared to MU01, peaking at a higher  $n_{e,up}$ , at the start of the outer leg radiative detachment ( $\hat{L}_{peak} > 0$ ) and the inner separatrix radiation reaching the X-point ( $\hat{L}_{50\%}$   $\approx$  1). The relative decrease of confinement time is similar to MU01, with a reduction by ~half when the baricentre of the emission goes from  $\Psi_N = 1$  to 0.98. However, particle detachment (e.g. the outer target particle flux rollover) happens at a higher  $n_{e,up}$  than the confinement peak. This implies that, in this scenario, even if good core performance can be maintained with significant impurity radiation present at the X-point, achieving particle flux roll-over on the outer target through core fuelling requires a degradation of confinement in this conventional divertor scenario — consistent with previously observed TCV results [41]. It should be noted, however, that this has not been observed in the Super-X divertor (studied elsewhere) - which sustained particle flux detachment without deteriorating core performance [23].

The results for the LFS fuelled MU03 beam heated L-mode shots are shown in Fig. 6. The up/down outer particle flux ratio is unchanged compared with Ohmic shots, but both particle fluxes are increased due to the higher  $P_{SOL}$ . The outer target ion flux increases initially more sharply than observed in the Ohmic cases, likely because the initial density achieved is lower and  $P_{SOL}$  is significantly higher. Because of this, the ion target flux evolution shows a clearer roll-over, although occurring at similar core and upstream densities. Because of the higher core density, the gradient in the SOL is larger, resulting in a larger uncertainty of  $n_{e,up}EFIT$ . This can also be observed in a larger spread of the data. Due to the lower  $n_{e,up}$ /higher  $P_{SOL}$  starting point, it is possible to observe the inner leg  $\hat{L}_{peak}$  unstable transition from the target to the X-point, consistent with the DLS model prediction. The  $\hat{L}_{peak}$  detachment does not seem to be reliably observed on the outer leg, indicating that it happens there at lower  $n_{e,up}$  as here achieved. Differently from the Ohmic case, the outer and inner legs 50% falloff marker movement happens at about the same density as the particle flux roll-over. This suggests that the difference of  $\hat{L}_{peak}$  detachment between inner and outer leg could be due to differences in carbon sputtering or impurity transport. The interpretation of DMS and MWI data is similar to ohmic shots, with  $\hat{L}_{50\%}$  detachment at the same time as  $D_2$  Fulcher emission reduction. The XPI/MWI  $D_2$  Fulcher emission inversions show a similar behaviour on the outer leg as in Ohmic shots, with the  $D_2$  Fulcher emission detaching together with the  $\hat{L}_{50\%}$ radiation marker. On the inner leg, instead  $D_2$  Fulcher emission, albeit showing the usual jump from target to X-point, seems to start detaching earlier than previously observed, especially in shot 49408. This could be due to a steeper temperature gradient, given the higher upstream temperature and power. The energy confinement time profile evolution is quite similar to the MU03 Ohmic case, peaking while  $\hat{L}_{50\%}$  detaches on both legs. The penetration of the radiation in the core seems to have here a stronger effect than in the Ohmic case, as it reduces by ~ half with a reduction of  $\Psi_N$  from 1 to ~0.99. This could imply that the cooling of the separatrix reduces the power from the beams reaching the core, hence reducing the total core heating.

#### 7. Conclusion and future work

In this paper the first scientific results exploiting the new MAST-U infrared imaging bolometer (IRVB) are presented using L-mode conventional divertor density ramp discharges. The radiation in the inner divertor leg sharply transitions from near the target to near the X-point as density is increased both in terms of the peak radiation and the 50% falloff marker. In contrast, the radiation front detachment evolves gradually from the target to the X-point on the inner leg. The DLS model [12,17] suggests an unstable thermal front evolution in the inner leg and a stable thermal front evolution at the outer target, consistent with experiments. After or about at the same time as the 50% falloff radiation marker has detached from both targets, ultimately particle detachment is observed from the ion target flux roll-over.

The fuelling location can have a strong impact on the radiation evolution: fuelling from the HFS causes the emergence of a MARFE-like structure at the HFS midplane that can then penetrate the core and affect core performance, and an earlier detachment on both legs. LFS fuelling and reducing plasma surface interactions with the main vessel wall resulted in a much wider detachment window and higher core performance. The energy confinement time starts to degrade at lower upstream densities than required for particle flux detachment, but higher densities than required for the peak radiation to move upstream. This suggests that for these conventional divertor scenarios without extrinsic seeding, significant radiation close to the X-point does not impact the energy confinement time — but particle flux detachment needs such high densities that energy confinement starts to degrade.

Comparing observations between the IRVB and the  $D_2$  Fulcher emission from DMS, XPI, MWI diagnostics allowed to infer the relative importance of impurity and hydrogenic radiative losses, and its impact for detachment. Impurity losses mainly drive the movement of the peak radiation, while the 50% falloff marker is more closely aligned with the ionisation front.

Hardware upgrades for improved measurements are underway, including a replacement of the existing IRVB IR camera, enabling a higher time resolutions. In the next MAST-U vacuum breach, the foil will be replaced with a more uniform one [18], and a second IRVB installed aimed at the upper X-point, to assess up/down asymmetries and provide a full bolometric coverage of the entire plasma volume. Future experimental campaigns are planned to fill the gaps highlighted in this research. Starting from a lower initial upstream density (or higher power conditions) to radiatively attach both legs can reveal the importance of (intrinsic) impurity radiation on the outer leg. The upper IRVB can be used to investigate up/down asymmetries [39,40], to understand the impact of drifts and the significance of deviating from the ideal double null. It is also planned to investigate the impact of inner target geometry on the stability of the thermal front detachment, as the DLS model predicts the transition on the inner leg to change from sharp to more gradual going from a more horizontal to vertical leg.

# CRediT authorship contribution statement

Fabio Federici: Writing - original draft, Project administration, Investigation, Formal analysis, Data curation, Conceptualization. Matthew L. Reinke: Supervision, Conceptualization. Bruce Lipschultz: Supervision, Investigation, Conceptualization. Jack J. Lovell: Supervision, Project administration, Methodology, Investigation. Kevin Verhaegh: Writing - review & editing, Investigation. Nicola Lonigro: Data curation, Formal analysis, Investigation, Validation, Writing - review & editing. Cyd Cowley: Writing - review & editing, Methodology. Mike Kryjak: Writing - review & editing, Methodology, Investigation. Peter Ryan: Validation, Data curation. Andrew J. Thornton: Project administration, Funding acquisition. James R. Harrison: Project administration, Funding acquisition. Byron J. Peterson: Resources, Methodology. Bartosz Lomanowski: Writing - review & editing, Supervision, Investigation. Jeremy D. Lore: Writing - review & editing, Supervision, Investigation, Funding acquisition. Yacopo Damizia: Writing - review & editing.

<sup>&</sup>lt;sup>3</sup> In the inversions the outer separatrix is affected by significant artefacts, so the location of the markers becomes less reliable as radiation increases, hence only a few points are visible.

# Declaration of competing interest

The authors declare that they have no known competing financial interests or personal relationships that could have appeared to influence the work reported in this paper.

# Acknowledgements

This work is supported by US Department of Energy, Office of Fusion Energy Sciences under the Spherical Tokamak program, contract DE-AC05-00OR22725 and under the auspices of the EPSRC [EP/L016 63X/1]. Support for M. L. Reinke's contributions was in part provided by Commonwealth Fusion Systems.

This work has been carried out within the framework of the EU-ROfusion Consortium, funded by the European Union via the Euratom Research and Training Programme (Grant Agreement No 101052200-EUROfusion) and from the EPSRC [grant number EP/W006839/1]. Views and opinions expressed are however those of the author(s) only and do not necessarily reflect those of the European Union or the European Commission. Neither the European Union nor the European Commission can be held responsible for them.

# Data availability

Data will be made available on request.

# References

- [1] W. Morris, et al., IEEE Trans. Plasma Sci. 46 (5) (2018) 1217-1226.
- [2] G. Fishpool, et al., J. Nucl. Mater. 438 (SUPPL) (2013) S356-S359.
- [3] D. Moulton, et al., Nucl. Fusion 5 (2024) 1-50.
- [4] K.H. Verhaegh, et al., Nucl. Fusion 63 (1) (2022) 21.
- [5] K. Verhaegh, et al., Nucl. Fusion 63 (12) (2023).
- [6] J.F. Rivero-Rodriguez, et al., 45th EPS Conference on Plasma Physics, EPS 2018 2018-July, European Physical Society, 2018, pp. 233–236.

- [7] F. Federici, Ph.D. dissertation, University of York, 2023.
- [8] F. Federici, et al., Rev. Sci. Instrum. 94 (3) (2023) 033502.
- [9] V.A. Soukhanovskii, et al., Nucl. Mater. Energy 33 (2022).
- [10] S.S. Henderson, et al., Nucl. Mater. Energy (2024) submitted for publication.
- [11] F. Federici, et al., 70th Annual Meeting of the APS Division of Fluid Dynamics, Denver, 2023, p. 1.
- [12] B. Lipschultz, et al., Nucl. Fusion 56 (5) (2016).
- [13] A. Kallenbach, et al., Plasma Phys. Control. Fusion 55 (12) (2013).
- [14] P.C. Stangeby, Plasma Phys. Control. Fusion 60 (4) (2018) 044022.
- [15] K. Verhaegh, et al., Nucl. Fusion 64 (8) (2024) 086050.
- [16] O. Myatra, Ph.D. dissertation, University of York, 2021.
- [17] C. Cowley, et al., Nucl. Fusion 62 (8) (2022).
- [18] F. Federici, et al., Rev. Sci. Instrum. 95 (10) (2024).
- [19] S.A. Silburn, et al., Calcam (2020).
- [20] M. Bernert, et al., Nucl. Fusion 61 (2) (2021) 024001.
- [21] P. Stangeby, Ser. Series in Plasma Physics, Vol. 1, CRC Press, 2000, p. 43, (2).
- [22] I.H. Hutchinson, Nucl. Fusion 34 (10) (1994) 1337-1348.
- [23] K. Verhaegh, et al., Communications physics, 2025, in press, arxiv:2311.08586.
- [24] J. Harrison, G. Fishpool, A. Kirk, J. Nucl. Mater. 438 (2013) S375–S378, Proceedings of the 20th International Conference on Plasma-Surface Interactions in Controlled Fusion Devices.
- [25] J.R. Harrison, et al., Plasma Phys. Control. Fusion 61 (6) (2019) 065024.
- [26] T. Ravensbergen, et al., Nucl. Fusion 60 (6) (2020) 066017.
- [27] T.A. Wijkamp, et al., Nucl. Fusion 63 (5) (2023) 056003.
- [28] B. Kool, et al., Nature physics, 2025, in press, arxiv:2407.07784.
- [29] P.J. Ryan, et al., Rev. Sci. Instrum. 94 (10) (2023).
- [30] N. Osborne, et al., Plasma Phys. Control. Fusion 66 (2) (2024) 025008.
- [31] N. Osborne, et al., ArXiV pre-print, arxiv:2410.14403.
- [32] X. Feng, et al., Rev. Sci. Instrum. 92 (6) (2021).
- [33] N. Lonigro, et al., Presented At the 66th APS DPP Annual Meeting, 2024.
- [34] A. Kallenbach, et al., Nucl. Fusion 55 (5) (2015).
- [35] M.L. Reinke, 7th IAEA Technical Meeting on Steady State Operation of Magnetic Fusion Devices, 2013.
- [36] F. Reimold, et al., Nucl. Fusion 55 (3) (2015).
- [37] L.L. Lao, et al., Nucl. Fusion 25 (11) (1985) 1611-1622.
- [38] O. Février, et al., Nucl. Fusion 61 (11) (2021).
- [39] I. Paradela Pérez, Nucl. Fusion, Accept. (2025).
- [40] J.J. Lovell, et al., Nucl. Mater. Energy 41 (2024) 101779.
- [41] K. Verhaegh, et al., Nucl. Fusion 59 (12) (2019) 126038.